Optical assessment of tissue anisotropy in *ex vivo* distended rat bladders

Sanaz Alali
Karen J. Aitken
Annette Schröder
Darius J. Bagli
I. Alex Vitkin

Optical assessment of tissue anisotropy in *ex vivo* distended rat bladders

Sanaz Alali,[a] **Karen J. Aitken,**[b] **Annette Schröder,**[b] **Darius J. Bagli,**[b] **and I. Alex Vitkin**[a,c]

[a]University of Toronto, Division of Biophysics and Bioimaging, Ontario Cancer Institute/University Health Network and Department of Medical Biophysics, 610 University Avenue, Toronto, Ontario M5G 2M9 Canada

[b]University of Toronto, Division of Urology, Developmental & Stem Cell Biology, Sick Kids Hospital, 555 University Avenue, Toronto, Ontario M5G 1X8 Canada

[c]University of Toronto, Department of Radiation Oncology, 610 University Avenue, Toronto, Ontario M5G 2M9 Canada

Abstract. Microstructural remodelling in epithelial layers of various hollow organs, including changes in tissue anisotropy, are known to occur under mechanical distension and during disease processes. In this paper, we analyze how bladder distension alters wall anisotropy using polarized light imaging (followed by Mueller matrix decomposition). Optical retardance values of different regions of normal rat bladders under different distension pressures are derived. Then optical coherence tomography is used to measure local bladder wall thicknesses, enabling the calculation of the tissue birefringence maps as a measure of the tissue anisotropy. Selected two-photon microscopy is also performed to better understand the compositional origins of the obtained anisotropy results. The dome region of the bladder shows maximum birefringence when the bladder is distended to high pressures, whereas the ventral remains roughly isotropic during distension. In addition, the average anisotropy direction is longitudinal, along the urethra to dome. The derived wall anisotropy trends are based on birefringence as an intrinsic property of the tissue organization independent of its thickness, to aid in understanding the structure-functions relation in healthy bladders. These new insights into the wall microstructure of *ex vivo* distending bladders may help improve the functionality of the artificially engineered bladder tissues. © *2012 Society of Photo-Optical Instrumentation Engineers (SPIE).* [DOI: 10.1117/1.JBO.17.8.086010]

Keywords: polarized light imaging; retardance; birefringence; anisotropy; bladder, urology; nonlinear microscopy; optical coherence tomography.

Paper 12037 received Jan. 16, 2012; revised manuscript received Jun. 14, 2012; accepted for publication Jul. 17, 2012; published online Aug. 17, 2012; corrected Oct. 12, 2012.

1 Introduction

In several diseases such as bladder obstruction, spinal cord injuries and diabetes, normal bladder function changes as a result of bladder wall morphology alterations.[1–6] Although these are known to be the main reason for bladder dysfunction, their exact relation to altered bladder functionality is still unclear.[4] Bladder wall is composed of extracellular matrix (including collagen and elastin) and smooth muscle.[7] During outlet obstructive diseases, the bladder wall experiences smooth muscle overgrowth (hypertrophy and hyperplasia) or changes in smooth muscle cell orientation, an increase in total wall thickness, and excessive extracellular matrix deposition and remodelling.[1,3] In many cases, over the long-term these alterations become irreversible, decrease patient quality of life, and increase risk of kidney failure and urinary tract infections. One promising solution is replacing the bladder with engineered tissues.[8,9] A major outstanding issue in this approach is ensuring comparable functionality through comparable engineered architecture, required for a healthy normal bladder. Thus, currently ambiguous relationships between distension-induced changes in the organization of smooth muscle and extracellular matrix tissues that comprise the bladder wall, and the resulting alterations in bladder function, warrant further investigation.

Several groups have taken a biomechanical characterization approach in quantifying the bladder wall displacement (strain) and correlating it to the liquid pressure inside the bladder. Korossis et al.,[10] mechanically stretched trabeculae from different regions of porcine bladder, and based on the resultant thickness changes in different directions, identified regions with distinct anisotropy and elasticity. To relate the anisotropy to the pressure inside the bladder, approximations such as a spherical bladder shape have been assumed, and Laplace's law has also been invoked to describe pressure-shape relationships.[10] In a recent study, displacement has been measured from the surface of the bladder wall while bladders were distended *ex vivo* under controlled pressure and volume of liquid,[11] from which regional anisotropy and strain have been calculated using Laplace's law. Although such displacement measurements coupled with biomechanical models are useful to detect elasticity and anisotropy, they do not provide any information on the underlying tissue organization. Therefore, this missing organizational information about bladder wall morphology and microstructure is acquired from thin samples using optical microscopy techniques.[10,12]

Polarized light imaging in bulk intact tissues is beginning to be used for quantitative assessment of morphology in biological tissues.[13–20] When the tissue polarimetric properties are properly decoupled with the help of polarization data analysis technique known as polar Mueller matrix decomposition,[21,22] a particular parameter known as retardance emerges. Retardance is a

Address all correspondence to: Sanaz Alali, University of Toronto, Division of Biophysics and Bioimaging, Ontario Cancer Institute/University Health Network and Department of Medical Biophysics, 610 University Avenue, Toronto, Ontario M5G 2M9 Canada. E-mail: sanaz.alali@utoronto.ca

measure of tissue anisotropy, which reports on its organized/ disorganized nature. It is a product of tissue optical birefringence and sampled tissue thickness. Some tissues are known to be anisotropic (birefringent) in their normal functional state.[19,23,24] For example, polarized light imaging has been utilized to determine the micro-structural organization in cardiac muscle, including its alterations due to infarct and post-infarct recovery induced by stem-cell therapies.[17] Cardiac anisotropy was shown to decrease with infarct formation (disorganized collagen scar tissue), and recover towards near-normal anisotropic levels with various forms of regenerative stem-cell therapies.[17,25,26] Furthermore, birefringence can be induced by mechanical forces (strain) in most materials, including biological tissues.[16] In fact, strain induces additional organization, which can be detected optically as birefringence. Birefringence in a distending bladder is a combination of both the birefringence due to intrinsic tissue organization and the strain induced organization.

In this study, we use polarized light imaging to obtain local maps of bladder birefringence (from polarimetry-derived retardance images, normalized by the bladder wall thickness measured with optical coherence tomography). This potential metric of bladder functional status varies spatially in normal bladders and in its regional response to bladder filling pressure, as characterized in this study. We also perform selected nonlinear microscopic examinations of the bladder wall, to help understand the polarimetric findings of bladder anisotropy. We believe our results are the first systematic optical characterization studies of normal *ex vivo* bladder microstructural/ organizational changes as related to distension pressure.

2 Materials and Methods

2.1 *Ex vivo Bladder Harvesting and Distension*

Female Sprague-Dawley rats were anaesthetised under isofluorane, the abdomen was opened and the bladders were exposed.[7,27] A simple anatomical representation of the bladder and a photo of the *ex vivo* harvested bladder are shown in Fig. 1. The ureters were ligated with a 5-0 blue viacryl suture on the right side of the rat and with a black 8-0 silk suture on the left. This simple colour coding enabled proper orientation of the bladder after harvesting. The urethra was catheterized with a 20-0 angiocatheter and the urethra sutured around the catheter with 4-0 silk suture, in four separate locations. The bladder and urethra were removed carefully from the animal, which was then sacrificed under anaesthesia according to an institutionally approved animal use protocol. The catheterized bladders were then placed in cell culture medium, phenol red-free Dulbecco's Modified Eagle' Medium (MEM), prior to distension.[27,28]

To distend the bladders, we used varying pressure head, by varying the height of the liquid reservoir coupled to the bladder via the urethra [Fig. 2(a)]. To ensure that the polarimetric signal was coming from the illuminated spot on the bladder wall, we had to minimize the reflection and scattering from sidewalls and distal portions of the bladder wall; to do so, the liquid in the reservoir-bladder system was a mixture of crimson blue dye dissolved in ethanol (to prevent contributions from bladder regions other than the illuminated region) and oil (to prevent the dye from penetrating into the bladder wall and thus altering the wall tissue optics). This mixture has been optimized empirically, ensuring ~1.5 *h* before the bladder wall begins to absorb the dye. For this reason and also to make sure that we are testing the bladders in their fresh condition, all imaging measurements were performed within 1 h. The density of the liquid mixture was measured to be 0.747 g/cm³. The pressure P at the top of the bladder (at the urethra) was then determined according to $P = \rho g h$, where ρ is the oil-dye density, h is the reservoir height and g is the acceleration due to gravity. Three bladders (referred to as 1, 2, and 3 in the text) were distended at three different reservoir heights of 15, 30, and 45 cm, corresponding to pressures of 1.0, 2.2, and 3.3 kPa; this range of pressures in within the relevant physiologic range.[7] With this method, we could image bladder 1 distended at 1.0 kPa, bladder 2 at 2.2 kPa and bladder 3 at 3.3 kPa. This was done instead of distending a single bladder to three different pressures, to avoid any possible hysteresis effects.

2.2 *Polarized Light Imaging*

To derive the retardance (and from that the intrinsic tissue birefringence, as a measure of its anisotropy) of the distended bladders, we used polarized light imaging in reflection mode [Fig. 2(b)]. A 635 nm diode laser (Thorlabs, Newton, New Jersey) was used as the light source. We generated four different incident polarization states (three linear and one right circular) using a
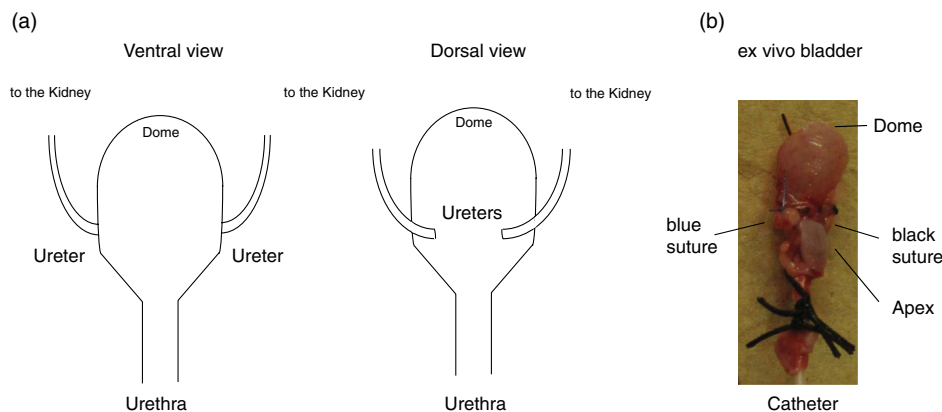

Fig. 1 (a) Ventral and dorsal schematics of the bladder anatomy. Urine enters from the kidneys via the ureters, and exits via the urethra. Clinical obstructions often occur at the urethra. (b) photograph of an *ex vivo* catheterized bladder. Various bladder structures and regions—dome, apex, ureters and urethra—are identified in the figure. The blue and black sutures indicate the ureters, this colour marking helping to determine the proper bladder orientation (dorsal/ventral) after harvesting.
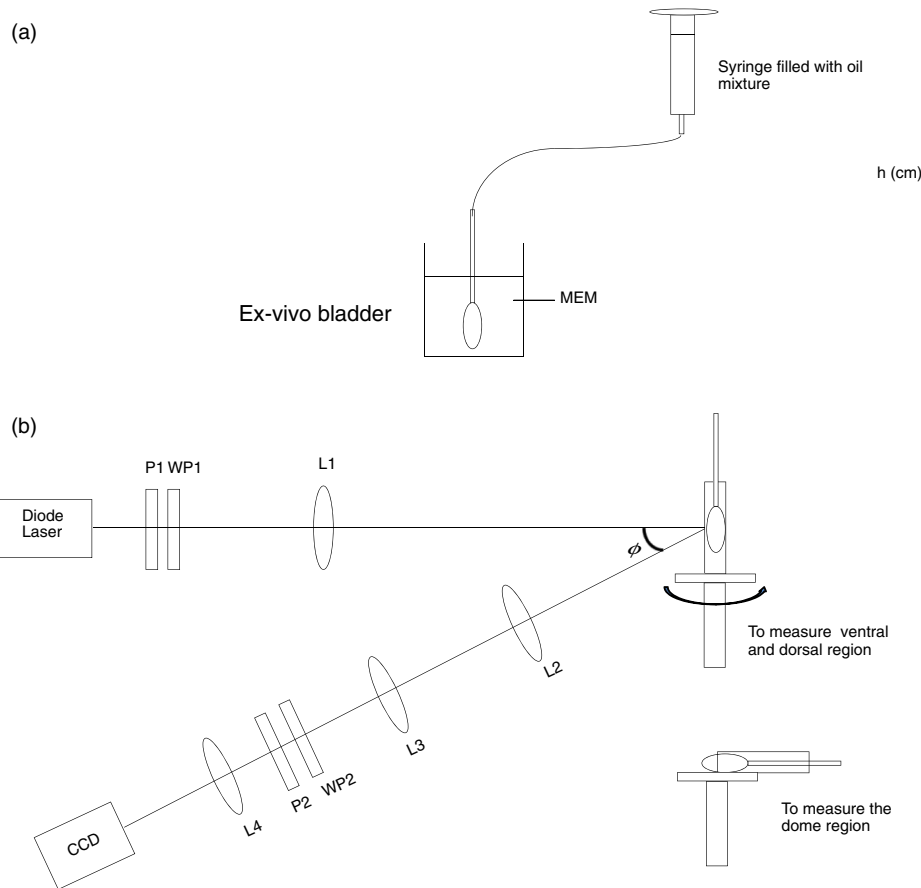
Fig. 2 (a) Arrangement for *ex vivo* bladder distension, the bladder was kept in phenol red-free Dulbecco's Modified Eagle' Medium (MEM) during distension. (b) Polarized light imaging set up. P1 and P2 are polarizers, WP1 and WP2 are waveplates, L1, L2, L3, and L4 are lenses. The bladder was placed on a rotational stage. ϕ was set to 25 deg.

waveplate and a polarizer for the sample illumination. The *ex vivo* bladders were placed on a rotational mount. The light spot on the bladder was ∼3 mm in diameter. Several spots in each anatomical bladder region (dorsal, ventral, and dome) were imaged by rotating the bladder. The imaging was not performed in the regions close to the sutures, since these likely exhibit strain anisotropy induced by the surgical preparation. The angle between the incident beam and collected backscattered light was 25 deg off the exact backscattering direction. Six different output polarization states (four linear and two circular) were collected using a polarizer and a waveplate. The polarized light images were detected by a CCD camera (CoolSNAPK4, Photometrics, Tuscon, Arizona). From this 24-measurement methodology (four input and six output polarization states), Mueller matrices were calculated at different regions of the bladder at three different distension pressures.[17]

The measured Mueller matrix contains several sample polarization effects occurring simultaneously intermixed in a complex way in its 16 elements. One way to extract intrinsic constituent components of potential biological/biophysical significance is to use a technique known as polar decomposition.[22] In particular, a Lu-Chipman decomposition approach has been used to decompose the Mueller matrix into its constituent basis matrices and extract individual polarization effects from these.[22,25,29] We have adopted this method for biophotonic applications, validated it with phantoms and Monte-Carlo simulations, and successfully used it in biological tissues.[25,29] The

experimentally measured bladder Mueller matrix was therefore decomposed into the product of three constituent 'basis' matrices: a diattenuator matrix M_D, a retarder matrix M_R, and a depolarizer matrix M_Δ. Mathematically, this can be written as:

$$M = M_\Delta M_R M_D. \tag{1}$$

Although other multiplication orders are possible, the results for biological tissues are essentially unaltered.[30] From M_R, one can obtain the sample linear retardance as:

$$\delta = \cos^{-1}\{[(M_R(2,2) + M_R(3,3))^2 + (M_R(3,2) - M_R(2,3))^2]^{1/2} - 1\}, \tag{2}$$

where δ represents the cumulative relative phase shift incurred by the orthogonal light polarization components in traversing the sample. The retardance matrix M_R can be further decomposed into the product of linear retardance M_{LR} and the optical chirality M_Ψ. θ the orientation of the anisotropy axis (fast axis direction), projected on the plane perpendicular to the incident beam, can be obtained from the M_{LR} elements as:[31]

$$\theta = 0.5 \tan^{-1}\left[\frac{M_{LR}(4,2) - M_{LR}(2,4)}{M_{LR}(3,4) - M_{LR}(4,3)}\right]. \tag{3}$$

As mentioned, polar decomposition allows the extraction of the magnitude [Eq. (2)] and dominant orientation [Eq. (3)] of the linear retardance of the interrogated tissue. However, we are interested in bladder intrinsic birefringence (a measure of its anisotropy), and not just retardance, as the latter is influenced by thickness in addition to anisotropic (micro-organizational) changes. The governing equation relating retardance δ to both sample intrinsic birefringence Δn and its thickness (in our case, the optical pathlength d that the backscattered detected photons have traveled) is:

$$\delta = (2\pi/\lambda)\Delta n d, \tag{4}$$

where λ is the light wavelength. Knowing the exact pathlength d in different measurement geometries is challenging, in part due to tissue multiple scattering effects (which preclude a unique value of d, but rather yield a statistical distribution of photon paths, from which various averaged quantities of interest (e.g., average pathlength) can be derived). Hence, absolute birefringence results in backscattering, or most other geometries, are rarely reported. However, average pathlength of photons can be estimated using polarization sensitive Monte Carlo simulations knowing the tissue's optical properties and the imaging geometry.[32–34] We have measured the rat bladder's optical properties using the spatially resolved steady state diffused reflectance method described in Kim et al.[35] The average value reduced scattering coefficient in normal rat bladders at 635 nm was $\mu_s' = 7 \pm 1$ cm^{-1}, giving a transport mean free path of 0.14 cm.[36] We have run polarization sensitive Monte Carlo simulations for slabs with the rat bladder optical properties and with different wall thicknesses. Figure 3 demonstrates the averaged pathlength d that the polarization preserving photons (detected at 25 deg off backscattering axis) travel in a rat bladder wall of thickness L. As illustrated in Fig. 3, the average pathlength is about five times the transport mean free path and increases with the increase in the bladder wall thickness. Having thus obtained d (from OCT and Monte Carlo
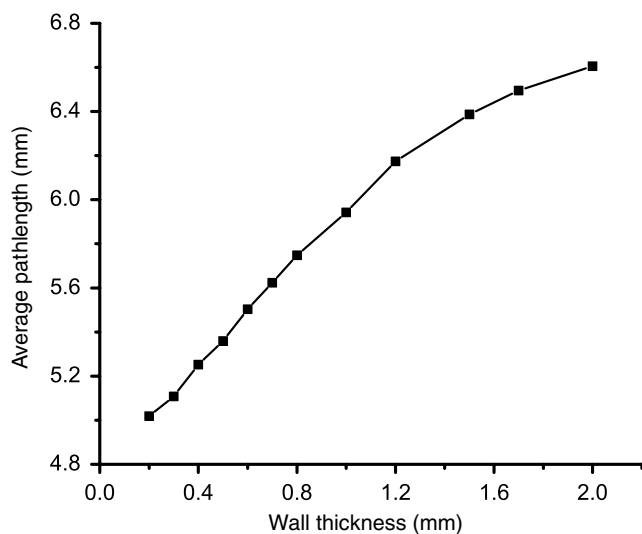

Fig. 3 The average pathlength d (mm) that the polarized photons (detected at 25 deg backscattering direction relative to the illumination direction) have traveled in the bladder wall as function of the bladder wall thickness L (mm). Symbols are results of polarization sensitive Monte Carlo simulations; line is a guide for the eye.

modelling) and δ from polarimetry, we can derive birefringence from Eq. (4).

Note that the derived birefringence values may be smaller than the true tissue birefringence; we are, in fact, measuring its projection onto the plane perpendicular to the imaging axis. Thus the apparent birefringence $\Delta\bar{n}_{app}$ will be different at different detection angles ϕ.[37] Here we keep the measurement angle ϕ fixed at 25 deg reflection mode, and report differences in apparent tissue birefringence from different bladder regions and under different distension pressures. However, we have developed methods to derive the true Δn that require additional angular projections,[37] and these will be applied to the bladder distension studies in future publications.

The linear retardance driven from Eq. (2) is the net retardance of the tissue. However, biological tissues are heterogeneous and the fiber alignments usually vary in spatial micro-domains, often as a function of depth (i.e., different anisotropy orientations in different bladder wall layers). Therefore, the detected net retardance might be smaller than the real retardance of each layer. Yet it is well known that a stack of retarders with different fast axis orientations results in a total nonzero circular retardance; giving an indication if a derived low net retardance value is due to true tissue isotropy or instead caused by this anisotropic heterogeneity effect. Retardance in general can be written as a combination of linear and circular contributions and can be described by the retardance vector as:[22,38]

$$\vec{R} = R(1, a_1, a_2, a_3)^T, \tag{5}$$

where its magnitude and normalized fast axis can be calculated from M_R as:[22,38]

$$R = \cos^{-1}\left[\frac{tr(M_R) - 1}{2}\right], \tag{6}$$

$$a_i = \frac{1}{2\sin R}\sum_{j,k=1}^{3}\varepsilon_{ijk}[m_R(j,k)], \tag{7}$$

where ε_{ijk} is the Levi-Civita symbol.[22] Linear retardance is the sum of the retardances along a_1 and a_2; circular retardance (along a_3) is not a real phase shift between polarization states and instead appears as a rotation (like an optical activity effect). This geometric phase, also known as Pancharatnam phase or Berry's phase, occurs when the polarization states are transformed in different local coordinates.[38] Knowing that the retardance vector itself can be regarded as a Stokes vector, we can define its ellipticity angle as:

$$E = \frac{1}{2}\tan^{-1}\left(\frac{a_3}{\sqrt{a_1^2 + a_2^2}}\right). \tag{8}$$

The larger the magnitude of E, the larger is the difference between the fast axis orientations of the layers in the heterogeneous tissue. Hence, we can use ellipticity angle to detect regions of the bladder wall with depth-dependent varying fiber alignments.

2.3 Optical Coherence Tomography

To measure the regional thickness of the bladder wall, we used our recently developed Fourier-domain OCT system.[39,40]

The system is based on Mach-Zehnder interferometer; the source is a frequency domain mode locked fiber-ring laser with a center wavelength at 1310 nm and a sweep rate of 43 to 67 kHz. A polygon based filter is used to sweep a 112 nm wavelength range. The coherence length is 12 mm, the axial resolution is 9 μm in biological tissues, and the average power is 48 mW. We acquired the B-mode cross-sectional OCT images the bladder wall. The *ex vivo* distended bladders were placed under the OCT probe and several images from different regions were acquired by changing the bladder position. The catheter was inside the bladder in all the experiments and the bladder was filled with the oil-dye mixture to the predetermined distension level.

2.4 Multiphoton Microscopy

Multiphoton microscopy has been used in previous studies to investigate the morphology of the bladder wall.[12,41,42] Similarly, we have used mulitphoton microscopy to shed light on the underlying causes of the obtained polarimetric anisotropy signals and gain some information on interrogated tissue composition.[43] A Zeiss LSM 510 microscope (META NLO, Oberkochen, Germany) with a 63× water immersion objective lens was used to focus a mode locked Ti:sapphire laser at 800 nm. Depth of field was approximately 2 μm and lateral field of view was $140 \times 140 \times \mu m^2$. The second harmonic generation (SHG) signal, purported to originate primarily from collagen, was collected at 400 nm, in a wavelength window of ± 10 nm. The two photon excited fluorescence (TPEF) signal was collected from a spectral window of 430 to 570 nm, and likely represents both smooth muscle and elastin. To flatten the tissue for microscopic examinations, the distended bladder was cut along the apex to dome (see Fig. 1), and placed on a glass coverslip (no top coverslip to flatten the tissue was used, to avoid mechanical artefacts). In order to inhibit the nerve fiber response to slicing and consequently prevent smooth muscle contraction, Oxybutynin was added to the bladder prior to cutting.[44] The images were taken in reflection mode, at a depth of about 50 μm below the outer surface of the bladder wall.

3 Results and Discussion

To quantify the distension pressure/wall thickness relationship, we performed OCT imaging of bladder 1 at 1 kPa, bladder 2 at 2.2 kPa and bladder 3 at 3.3 kPa. Figure 4 shows representative B-mode OCT images, from the dome region of the three bladders. The effect of decreasing wall thickness with increasing distension pressure is evident in these images.

The bladder wall thickness is not as uniform as may appear from the OCT images in Fig. 4. Moving several millimetres to a
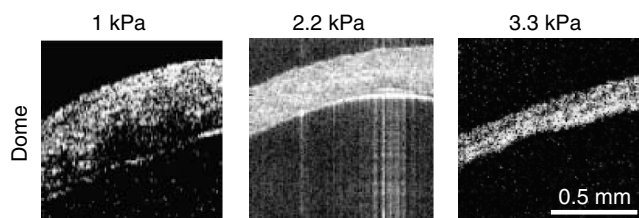

Fig. 4 Representative OCT B-mode structal images of the dome region in the three bladders distended to three different pressures to enable thickness determination.
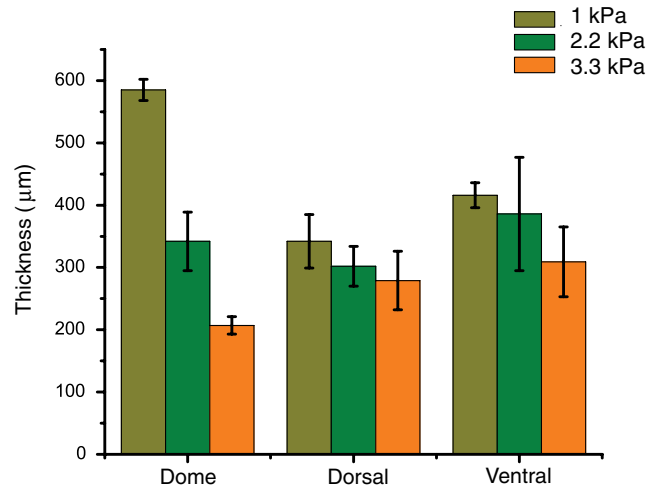

Fig. 5 Average wall thickness of different regions at three different distension pressures obtained from the structural OCT images. Error bars represent the standard deviation of the mean value (averaged over $\sim 3 \times 3$ mm^2 region).

different spot but still remaining within the same anatomical bladder 'zone' (dorsal/ventral/dome) gave rise to ~20% wall thickness variation. The mean values of regional wall thicknesses averaged over ~3 × 3 mm^2 area of each bladder are shown in Fig. 5. Note the varying magnitude of this effect in different bladder regions: dome exhibit larger thickness decreases than the dorsal and the ventral zones.

As seen in Fig. 5, increasing distension pressure decreases dome thicknesses significantly, but has only minimal effect on the ventral and dorsal wall; specifically, the ventral wall becomes the thickest bladder wall structure at 3.3 kPa. We have examined additional distended bladders (results not shown); although actual numbers vary, the above trends are consistent. Now with this bladder thickness information in hand, we can look up the average pathlength that the photons travel in each bladder wall from Fig. 3 and use it to calculate birefringence from the measured retardance [Eq. (4)].

It is important to note the possible variations in choosing the location of the spots in each zone on different bladders and therefore the necessity for our future studies to evaluate the whole bladder wall anisotropy for larger number of samples to reach statistically significant and clinically relevant results. In this paper, we have chosen illustrative spots with the highest retardance from each region of the distended bladders. The measured retardances varied from 15 deg to 160 deg for the dome, from 10 deg to 78 deg for the ventral and from 8 deg to 114 deg for the dorsal regions. We did not observe phase-wrapping in any of the examined spots. The anisotropy was then calculated using Eq. (4) for each spot. Note that usually anisotropy is gauged from the thickness change or displacement with the approximate assumption of spherical or ellipsoid shape of the examined structure.[10,11] In contrast, our approach enables the characterization of the bladder with respect to its optical anisotropy (birefringence), independent of its thickness and 'regular geometry' assumptions. Resulting images of regional anisotropy $\Delta \bar{n}_{app}$ are shown in Fig. 6. The images present 2 mm-diam circular fields of view, chosen from the highest signal to noise ratio (SNR) regions of each 3 mm-diam examined spot.
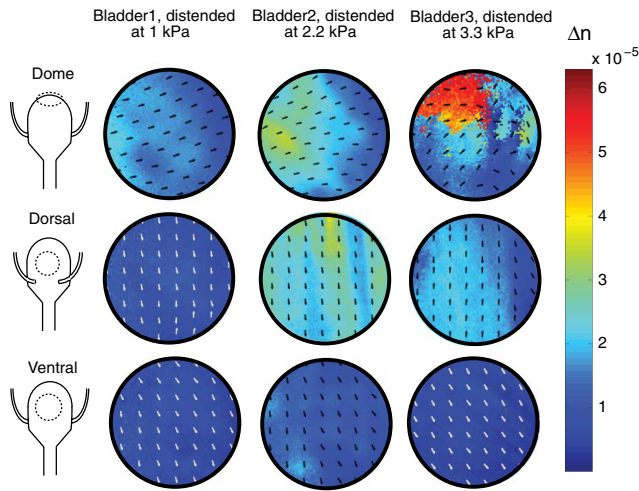
Fig. 6 Regional anisotropy (birefreingence) images of bladders 1, 2, and 3 (distended to 1.0, 2.2, and 3.3 kPa, respectively). The rows show the birefreingence images from the anatomical region indicated on the *ex vivo* bladder figure in the left column. The color represents the value of the anisotropy (color bar on right), the arrows indicate the anisotropy direction. The field of view is 2 mm in diameter.

Maximum anisotropy appears in the dome region distended at 3.3 kPa. The dome is not the most anisotropic region at low and mid pressures (1.0 and 2.2 kPa), but becomes more anisotropic as the pressure increases. Conversely, the ventral wall is nearly isotropic at low pressures, and remains so as the distension is increased. On the other hand, the dorsal wall anisotropy is significant at mid and high pressures. It can thus be concluded that the pressure-anisotropy behavior in dorsal and ventral regions differs from that in the dome region. Physiologically this seems reasonable, since the dome (the far region from the urethra) experiences high pressures when the bladder is almost full and probably shows its maximum compliance at the final filling stages. Also, the dome is known to be the most physiologically vulnerable area of the bladder to acute pressure insults, and is most prone to rupture.[45] Further, note that the regional anisotropy–pressure relationship does not follow the regional pressure-thickness correlation depicted in

Fig. 4. The polarimetry data hence implies that mechanical strain which results in distension and thickness change is not the only factor leading to change in anisotropy. Most likely, other factors such as organizational changes that are occurring in the different layers and regions of the bladder wall are also responsible for the observed anisotropy (birefringence) changes.

The net birefringence orientation (represented by arrows in Fig. 6) also shows interesting trends. Dorsal and ventral regions both exhibit anisotropic longitudinal alignment along the dome to the urethra. The longitudinal alignment is known to be the dominant direction of the smooth muscle layer as shown previously.[3] Therefore, we surmise that the dominant anisotropy in the bladder wall during distension is due to the stretching of the smooth muscle fibers. The orientation of the anisotropy in the dome follows the general orientation of the fibers in dorsal and ventral regions (note that the dome was examined in a horizontal position as shown in Fig. 2). However, at maximum pressure (~pathological level) the anisotropy orientations in the dome deviate from the rest of the dominant orientations in bladder wall. In order to explore the reason we evaluated the retardance ellipticity at this spot; recall that this is a metric of depth-dependent birefringence heterogeneity. As shown in Fig. 7, the retardance ellipticity is high at those regions with abnormal orientations. This indicates existence of spatial micro-domain retarders with different fast axis orientations throughout the depth, resulting in small values of net retardance and random like orientations. The retardance ellipticity angle for all other spots in Fig. 6 is lower than ~0.2 rad (about 20% of the ellipticity in Fig. 7), suggesting more uniform anisotropy orientation throughout those regions of the bladder wall.

Another interesting point is that although the average thicknesses of dorsal and ventral regions are similar during different distension pressures (Fig. 5) and they both exhibit dominant longitudinal orientations, their anisotropy values are very different at mid and high pressure (Fig. 6). One possible reason might be the differences in the extracellular matrix organization in these two regions; because as previously has been reported, the extracellular matrix organization and orientation alter during the bladder filling.[12,46] Thus, to elucidate the nature of the anisotropy–extracellular matrix micro-organization connection, we performed two-photon confocal microscopy at selected depths
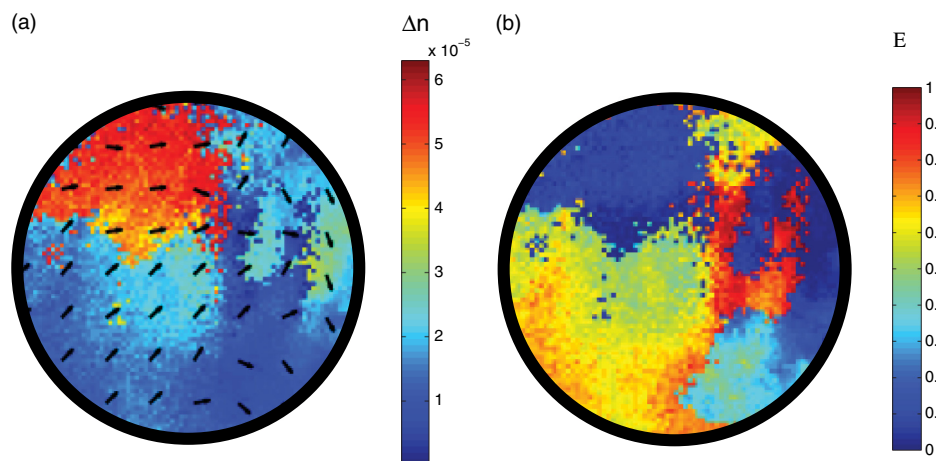

Fig. 7 Birefrience and retardance ellipticity angle images at a representative spot (2-mm-diam) from dome of the bladder distened to 3.3 kPa. (a) The birefringence image; scale bar shows the value of the birefringence and the arrows indicate the orientation of the fast axis, (b) the retardance ellipticity angle E image, the scale bar indicating the value of E.
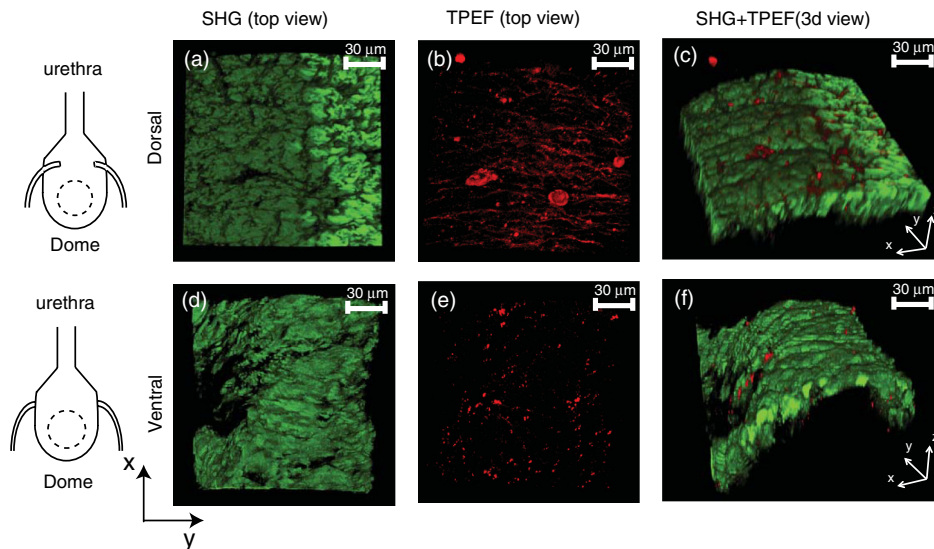
Fig. 8 Nonlinear microscopy images from representative spots from dorsal and ventral regions of a bladder distended at 3.3 kPa; about 25 adjacent slices, each 2 μm thick, were acquired above and below the central plane at 50 μm, (a) and (d) the green pseudocolor represent SHG signal indicating collagen fibers, (b) and (e) the red pseudo-color TPEF signal represents smooth muscle and elastin (see text for identification and spectral detection details), (c) and (f) show 3D rendering of the combined TPEF and SHG signals.

in the dorsal and ventral regions at 3.3 kPa (high pressure). We were not able to keep the curvature of the dome (when distended) with Oxybutynin after cutting the fresh bladder, so our microscopy results are limited to looking at the differences between dorsal and ventral regions. A normal rat bladder was distended up to 3.3 kPa and depth resolved two-photon microscopy images with 2 μm thick slices (depth of field) were acquired from representative spots of its dorsal and ventral regions. To get some idea of the depth dependence of the tissue structures, the Z-stacks of depth resolved slices were acquired around a central plane at 50 μm depth. 3-D rendering of these slices are shown in Fig. 8, where the green colour codes the SHG signal (likely emanating from the collagen fibers), while red shows the TPEF signal (likely from the elastin and smooth muscle compartments—see Sec. 2 for details). The collagen content is not very different in the two regions of the bladder wall (at least at the examined depths); however, as seen in the 2-D (maximum intensity projection) top views (1st column of Fig. 8), it appears more densely packed in the dorsal compared to the ventral regions. On the other hand, the elastin/smooth muscle network in the dorsal area is highly organized compared to the ventral zone (2nd column of Fig. 8). Comparison of Figs. 6 and 8 thus suggests that the organized and compact nature of extracellular matrix in the dorsal wall enhances its birefringence (anisotropy) compared to the ventral structures. Note that deriving a dominant orientation for the extracellular matrix is not straightforward due to its complex three dimensional organization.

To fully explain the measured birefringence trends with nonlinear microscopy images would require that the latter be acquired throughout the entire polarimetry imaging depth (~entire bladder wall thickness), which is not technically possible. However, even these observed micro-structural differences support our speculation about the role of extracellular matrix organization in determining tissue anisotropy properties. From Figs. 6–8, we can note a regional correlation between distension pressure in the bladder and structural organization (morphology) in its wall. This relation may prove to be useful in improving tissue engineered bladders function. For example, Helse et al., have shown that mechanical stimulation of the *in vitro* tissue engineered bladders triggers elastin production and improves bladder compliance.[9] Knowing the regions of the bladder which possess high content of elastin (e.g., dorsal zone according to our results) and their organization, tissue engineers can apply the optimum mechanical stimulation. In addition, our results demonstrate that the different regions of *ex vivo* distended bladders exhibit very different (thickness independent) anisotropy. Achieving similar regional anisotropy/distension pressure trends in artificial bladders may serve to improve their functionality.

4 Conclusion

Using polarized light imaging for regional birefringence mapping and OCT for local thickness measurements, we examined organizational anisotropy in *ex vivo* distended rat bladders as a function of distension pressure. The dome region was seen to become most anisotropic with distension, whereas the ventral side remained roughly isotropic. The dorsal wall showed significant anisotropy at mid and high distension pressures. The dominant average direction of anisotropy in the bladders was longitudinal, along the dome-apex axis. As expected, depth resolved multiphoton microscopy of the *ex vivo* distended bladder revealed the difference in organization of the extracellular matrix in the dorsal and ventral regions of the bladder wall. Overall, the thickness—pressure relation, birefringence—pressure relation and microscopy data, all together suggest that anisotropy changes with micro-structural remodelling in the bladder wall as well as with mechanical strain (which is proportional to thickness change and distension). Since the bladder function (distension/contraction) is supported by the specific extracellular matrix organization of its wall, these initial results may prove useful in guiding the design and enhancing the functionality of tissue engineered bladders in order to assist bladder failure patients.

References

1. K. J. Aitken and D. J. Bagli, "The bladder extracellular matrix. Part II: regenerative applications," *Nat. Rev. Urol.* **6**(11), 612–621 (2009).
2. T. Berrocal et al., "Anomalies of the distal ureter, bladder, and urethra in children: embryologic, radiologic, and pathologic features," *Radiographics* **22**(5), 1139–1164 (2002).
3. J. Nagatomi et al., "Quantification of bladder smooth muscle orientation in normal and spinal cord injured rats," *Ann. Biomed. Eng.* **33**(8), 1078–1089 (2005).
4. A. Tubaro et al., "The effect of bladder outlet obstruction treatment on ultrasound-determined bladder wall thickness," *Rev. Urol.* **7**(Suppl. 6), S35–S42 (2005).
5. C. C. Wang et al., "Diabetes-induced alternations in biomechanical properties of urinary bladder wall in rats," *Urology* **73**(4), 911–915 (2009).
6. K. J. Aitken and D. J. Bagli, "The bladder extracellular matrix. Part I: architecture, development and disease," *Nat. Rev. Urol.* **6**(11), 596–611 (2009).
7. K. J. Aitken et al., "Mammalian target of rapamycin (mTOR) induces proliferation and de-differentiation responses to three coordinate pathophysiologic stimuli (mechanical strain, hypoxia, and extracellular matrix remodeling) in rat bladder smooth muscle," *Am. J. Pathol.* **176**(1), 304–319 (2010).
8. G. S. Jack et al., "Urinary bladder smooth muscle engineered from adipose stem cells and a three dimensional synthetic composite," *Biomaterials* **30**(19), 3259–3270 (2009).
9. R. L. Heise et al., "Generating elastin-rich small intestinal submucosa-based smooth muscle constructs utilizing exogenous growth factors and cyclic mechanical stimulation," *Tissue Eng. Part A.* **15**(12), 3951–3960 (2009).
10. S. Korossis et al., "Regional biomechanical and histological characterisation of the passive porcine urinary bladder: implications for augmentation and tissue engineering strategies," *Biomaterials* **30**(2), 266–275 (2009).
11. A. Pareke et al., "*Ex vivo* deformations of the urinary bladder wall during whole bladder filling: contributions of extracellular matrix and smooth muscle," *J. Biomech.* **43**(9), 1708–1716 (2010).
12. M. Murakumo et al., "Three-dimensional arrangement of collagen and elastin fibers in the human urinary bladder: a scanning electron microscopic study," *J. Urol.* **154**(1), 251–256 (1995).
13. S. L. Jacques, J. r. Roman, and K. Lee, "Imaging superficial tissues with polarized light," *Lasers Surg. Med.* **26**(2), 119–129 (2000).
14. W. Groner et al., "Orthogonal polarization spectral imaging: a new method for study of the microcirculation," *Nat. Med.* **5**(10), 1209–1212 (1999).
15. R. A. Oldenbourg, "New view on polarization microscopy," *Nature* **381**(Suppl. 2), 811–812 (1996).
16. R. K. Curtis and T. D. Tyson, "Birefringence: polarization microscopy as a quantification technique of human hair analysis," *J. Soc. Cosmet. Chem.* **27**(7), 411–431 (1976).
17. M. F. G. Wood et al., "Polarization birefringence measurements for characterizing the myocardium, including healthy, infracted, and stem-cell-regenerated tissues," *J. Biomed. Opt.* **15**(4), 047009 (2010).
18. S. G. Demos and R. R. Alfano, "Temporal gating in highly scattering media by the degree of optical polarization," *Opt. Lett.* **21**(2), 161–163 (1996).
19. S. L. Jacques, J. C. Ramella-Roman, and K. Lee, "Imaging skin pathology with polarized light," *J. Biomed. Opt.* **7**(3), 329–340 (2002).
20. M. R. Antonelli et al., "Mueller matrix imaging of human colon tissue for cancer diagnostics: how Monte Carlo modeling can help in the interpretation of experimental data," *Opt. Express* **18**(10), 10200–10208 (2010).
21. M. F. G. Wood et al., "Proof-of-principle demonstration of a Mueller matrix decomposition method for polarized light tissue characterization *in vivo*," *J. Biomed. Opt.* **14**(1), 014029 (2009).
22. S. Y. Lu and R. A. Chipman, "Interpretation of Mueller matrices based on polar decomposition," *J. Opt. Soc. Am. A.* **13**(5), 1106–1113 (1996).
23. V. J. Sankaran, T. Walsh, Jr., and D. J. Maitland, "Comparative study of polarized light propagation in biologic tissues," *J. Biomed. Opt.* **7**(3), 300–306 (2002).
24. G. Jarry, F. Henry, and R. Kaiser, "Anisotropy and multiple scattering in thick mammalian tissues," *J. Opt. Soc. Am. A.* **17**(1), 149–153 (2000).
25. N. Ghosh et al., "Mueller matrix decomposition for polarized light assessment of biological tissues," *J. Biophotonics* **2**(3), 145–156 (2009).
26. S. H. Li et al., "Elastin gene overexpression during cell therapy prevents scar expansion and ventricular dysfunction after a myocardial infarction," *J. Molec. Cell Cardiol.* (accepted).
27. K. J. Aitken et al., "Mechanotransduction of extracellular signal-regulated kinases 1 and 2 mitogen-activated protein kinase activity in smooth muscle is dependent on the extracellular matrix and regulated by matrix metalloproteinase," *Am. J. Pathol.* **169**(2), 459–470 (2006).
28. B. O. Backhaus et al., "Alterations in the molecular determinants of bladder compliance at hydrostatic pressures less than 40 cm H$_2$O," *J. Urolology* **168**(6), 2600–2604 (2002).
29. N. Ghosh, M. F. G. Wood, and I. A. Vitkin, "Mueller matrix decomposition for extraction of individual polarization parameters from complex turbid media exhibiting multiple scattering, optical activity, and linear birefringence," *J. Biomed. Opt.* **13**(4), 044036 (2008).
30. N. Ghosh, M. F. G. Wood, and I. A. Vitkin, "Influence of the order of the constituents basis matrices on the mueller matrix decomposition," *Opt. Commun.* **283**(6), 1200–1208 (2010).
31. M. A. Wallenburg et al., "Comparison of optical polarimetry and diffusion tensor imaging for assessing myocardial anisotropy," *J. Innovat. Opt. Health Sci.* **3**(2), 109–121 (2010).
32. D. Cote and I. A. Vitkin, "Robust concentration determination of optically active molecules in turbid media with validated three-dimensional polarization sensitive Monte Carlo calculations," *Opt. Express* **13**(1), 148–163 (2005).
33. X. Guo, M. F. G. Wood, and I. A. Vitkin, "Angular measurements of light scattered by turbid chiral media using linear Stokes polarimeter," *J. Biomed. Opt.* **11**(4), 041105 (2006).
34. X. Guo, M. F. G. Wood, and I. A. Vitkin, "Monte Carlo study of pathlength distribution of polarized light in turbid media," *Opt. Express* **15**(3), 1348–1360 (2007).
35. A. Kim et al., "A fiberoptic reflectance probe with multiple source-collector separations to increase the dynamic range of derived tissue optical absorption and scattering coefficients," *Opt. Express* **18**(6), 5580–5594 (2010).
36. V. Ntziachristos, "Going deeper than microscopy: the optical imaging frontier in biology," *Nat. Methods* **7**(8), 603–614 (2010).
37. M. A. Wallenburg et al., "Polarimetry-based method to extract geometry-independent metrics of tissue anisotropy," *Opt. Lett.* **35**(15), 2570–2572 (2010).
38. D. Goldstein, *Polarized light*, 2nd ed., Marcel Dekker, New York (2003).
39. G. Y. Liu et al., "High power wavelength linearly swept modelocked fiber laser for OCT imaging," *Opt. Express* **16**(18), 14095–14105 (2008).
40. A. Mariampillai et al., "Speckle variance detection of microvasculature using swept-source optical coherence tomography," *Opt. Lett.* **33**(13), 1530–1532 (2008).
41. S. M. Zue et al., "Multiphoton microscopy of unstained bladder mucosa based on two-photon excited autofluorescence and second harmonic generation," *Laser Phys. Lett.* **6**(1), 80–83 (2009).
42. R. Cicchi et al., "Time- and spectral-resolved two-photon imaging of healthy bladder mucosa and carcinoma in situ," *Opt. Express* **18**(4), 3840–3849 (2010).
43. M. A. Wallenburg et al., "Two-photon microscopy of healthy, infracted and stem-cell treated regenerating heart," *J. Biophoton.* **4**(5), 297–304 (2011).
44. J. L. Molher, "Relaxation of intestinal bladders by intravesical oxybutynin chloride," *Neurol. Urodyn.* **9**(2), 179–187 (1999).
45. J. P. Vaccaro and J. M. Brody, "CT cystography in the evaluation of major bladder trauma," *RadioGraphics* **20**(5), 1373–1381 (2000).
46. S. L. Chang et al., "Role of type III collagen in filling," *Neurourol. Urodyn.* **17**(2), 135–145 (1998).